ACS APPLIED MATERIALS & INTERFACES

www.acsami.org

Research Article

Coupling between Pyroelectricity and Built-In Electric Field Enabled Highly Sensitive Infrared Phototransistor Based on InSe/WSe_2/P(VDF-TrFE) Heterostructure

Christy Roshini Paul Inbaraj, Roshan Jesus Mathew, Raman Sankar, Hsia Yu Lin, Nian-Xiu Li, Yit-Tsong Chen, and Yang-Fang Chen*

Cite This: *ACS Appl. Mater. Interfaces* 2023, 15, 19121−19128

Read Online

ACCESS | Metrics & More | Article Recommendations | Supporting Information

ABSTRACT: The assorted utilization of infrared detectors induces the demand for more comprehensive and high-performance electronic devices that work at room temperature. The intricacy of the fabrication process with bulk material limits the exploration in this field. However, two-dimensional (2D) materials with a narrow band gap opening aid in infrared (IR) detection relatively, but the photodetection range is narrowed due to the inherent band gap. In this study, we report an unprecedented attempt at the coordinated use of both 2D heterostructure (InSe/WSe_2) and the dielectric polymer (poly(vinylidene fluoride-trifluoroethylene), P(VDF-TrFE)) for both visible and IR photodetection in a single device. The remnant polarization due to the ferroelectric effect of the polymer dielectric enhances the photocarrier separation in the visible range, resulting in high photoresponsivity. On the other hand, the pyroelectric effect of the polymer dielectric causes a change in the device current due to the increased temperature induced by the localized heating effect of the IR irradiation, which results in the change of ferroelectric polarization and induces the redistribution of charge carriers. In turn, it changes the built-in electric field, the depletion width, and the band alignment across the p−n heterojunction interface. Consequently, the charge carrier separation and the photosensitivity are therefore enhanced. Through the coupling between pyroelectricity and built-in electric field across the heterojunction, the specific detectivity for the photon energy below the band gap of the constituent 2D materials can reach up to 10^{11} Jones, which is better than all reported pyroelectric IR detectors. The proposed approach combining the ferroelectric and pyroelectric effects of the dielectric as well as exceptional properties of the 2D heterostructures can spark the design of advanced and not-yet realized optoelectronic devices.

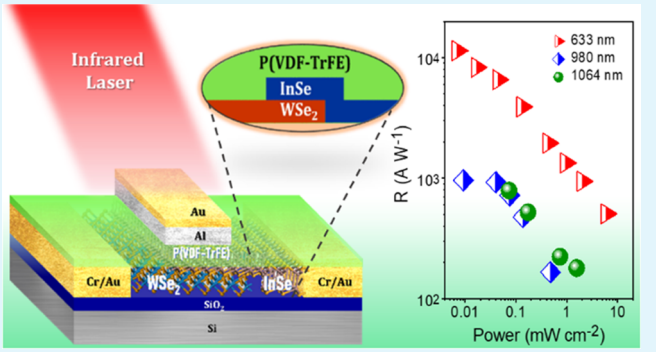

KEYWORDS: *pyroelectricity, 2D materials, InSe/WSe_2, van der Waals heterostructure, P(VDF-TrFE), ferroelectric gating, an infrared detector*

INTRODUCTION

Infrared (IR) photodetectors have attracted attention among researchers due to their extensive applications in remote sensing, optical communication, biomedical imaging, military surveillance, and chemical sensing.[1,2] According to the wavelength range, the IR (0.8−30 μm) region can be divided into the near-infrared (NIR), short-wave infrared (SWIR), mid-wave infrared (MWIR), long-wave infrared (LWIR), and far-infrared (FIR) range.[1] Due to the thermal noise and complicated device fabrication steps involved with IR photodetectors based on three-dimensional (3D) crystal structures so far, studies were focused on ultrathin two-dimensional (2D) materials for IR detection.[3,4] Mentioning 2D materials, graphene was the prime choice to experiment for IR photodetection by inducing a desirable band gap through doping.[1,5] Xia et al. demonstrated a graphene-based photodetector at 80 V gate bias for detecting 1.55 μm wavelength IR irradiation.[6] Consecutively, the next widely studied 2D transition metal dichalcogenide (TMD) MoS_2 was assembled with other TMDs to form a type II heterostructure (MoS_2/WS_2, MoS_2/$MoTe_2$) where the interband transition aids in IR absorption.[7,8] The $MoTe_2$/graphene/SnS_2 heterostructure to detect SWIR rays was demonstrated by Li et al.[9] Other 2D semiconductors like black phosphorous (0.3−2.0 eV), tellurium (0.3−1.0 eV), platinum diselenide ($PtSe_2$, 0−1.2

Received: December 21, 2022
Accepted: March 30, 2023
Published: April 7, 2023

eV), and palladium diselenide ($PdSe_2$, 0.1−1.2 eV) were studied to show promising results on IR photodetection.[1,3,10−12] The $PdSe_2/MoS_2$ heterostructure was reported by Long et al. for LWIR detection.[3] Besides assembling 2D layers, zero-dimensional (0D) materials like quantum dots, nanoparticles, and one-dimensional (1D) carbon nanotubes (CNT) were also combined with 2D materials for IR detection.[13−15] Hybrid structures like the graphene/CNT layer and MoS_2/HgTe quantum dots were also reported to detect the SWIR range.[15,16]

Despite assuring outcomes with specific 2D materials and their hybrid structures, the range for IR photodetection is limited according to the inherent nature of the band gap of the material. In this case, if the thermal heating effect of IR rays is taken advantage of, the range for IR detection can be increased, which will widen the application areas as well. The heat caused by IR rays causes a change in temperature over the irradiated area to which certain materials exhibit a change in net polarization in the material due to the pyroelectric effect.[17] Poly(vinylidene fluoride) (PVDF) is one such material to possess a pyroelectric effect.[18] PVDF copolymerizes with trifluoroethylene (TrFE) to form P(VDF-TrFE), which is a ferroelectric polymer that exhibiting both pyroelectric and piezoelectric effects.[19] Employing P(VDF-TrFE) as a dielectric to a device aids in IR detection by measuring the change in current caused by the change in dielectric polarization, and it can also be used as a ferroelectric transistor.

In this work, we will make an unprecedented attempt to demonstrate the coupling between pyroelectricity and a built-in electric field for a highly sensitive IR phototransistor consisting of P(VDF-TrFE) and a 2D van der Waals heterostructure to harvest both the optoelectronic property of 2D heterojunction for visible light photodetection and the pyroelectric effect of P(VDF-TrFE) for IR detection. Although there are few reports on ferroelectric gated 2D material transistors, there have been no studies on a pyroelectric gated 2D heterostructure. Here, we chose the type II $InSe/WSe_2$ heterostructure for our study, and there are limited reports on InSe-based heterostructures.[20,21] InSe is an n-type semiconductor with a band gap of 1.27 eV for a thickness of more than 6 nm and an electron mobility of 10^3 $cm^2/(Vs)$, whereas WSe_2 is a p-type semiconductor with a direct and indirect optical transition based on the number of layers and has a carrier mobility of 10^2 $cm^2/(Vs)$.[22−25] The $InSe/WSe_2$ heterostructure top-gated with P(VDF-TrFE) dielectric shows an ambipolar transfer behavior, and the ferroelectric polarization results in a relatively higher photoresponsivity (λ = 633 nm) in the polarized state (10^4 A W^{-1}) than the unpolarized state. During IR irradiation (λ = 980, 1064 nm) in the polarized state, due to the pyroelectric effect in P(VDF-TrFE), a significant change in current was observed for different laser power intensities, which is indicative of the enhanced IR detection. The underlying mechanism of enhanced photosensitivity arises from the existence of the built-in electric field across the heterojunction. Under IR irradiation, the increased temperature will induce the change of the PVDF polarization as well as the built-in electric field, which enables the alteration of depletion width, changes the band alignment across the heterojunction, and varies the charge carrier separation. As a result, the photosensitivity is enhanced, and the specific detectivity for the photon energy below the band gap of the constituent 2D materials can reach up to 10^{11} Jones, which is better than all the reported pyroelectric IR detectors.

RESULTS AND DISCUSSION

Figure 1a represents the schematic illustration of the $InSe/WSe_2$ device on a SiO_2/Si substrate with ferroelectric P(VDF-TrFE) film as the top dielectric layer. InSe and WSe_2 crystals were grown by the vertical Bridgman technique and chemical vapor transport (CVT) method, respectively. The growth procedures were detailed in our previous report.[26] The as-grown InSe crystal belongs to the β phase and has a hexagonal structure.[26,27] The layered WSe_2 crystals also have a hexagonal crystal structure.[26] Both the crystals were exfoliated into ultrathin flakes by a mechanical exfoliation technique. The exfoliated WSe_2 flakes were transferred to the SiO_2/Si substrate with a poly(dimethylsiloxane) (PDMS) stamp. In the same manner, InSe flakes were precisely assembled on top of WSe_2 to form a heterojunction. The assembled heterostructure was coated with P(VDF-TrFE) solution after depositing electrodes and then annealed. The detailed device fabrication steps involved along with the schematic are given in Supplementary Note 1. The optical microscope image of the stacked $InSe/WSe_2$ heterojunction device is shown in Figure 1b. The atomic force microscopy (AFM) image with the height profile is represented in Figure 1c. The thicknesses of InSe and WSe_2 flakes were determined to be ∼21 and ∼19 nm, respectively. To obtain ambipolar or anti-ambipolar transport behavior in a heterostructure where comparable electron and hole contributions play a major role, it is necessary to have similar levels of intrinsic carrier density in both p- and n-type material.[28,29] Otherwise, the asymmetry can lead to the domination of either of the carrier resulting in unipolar

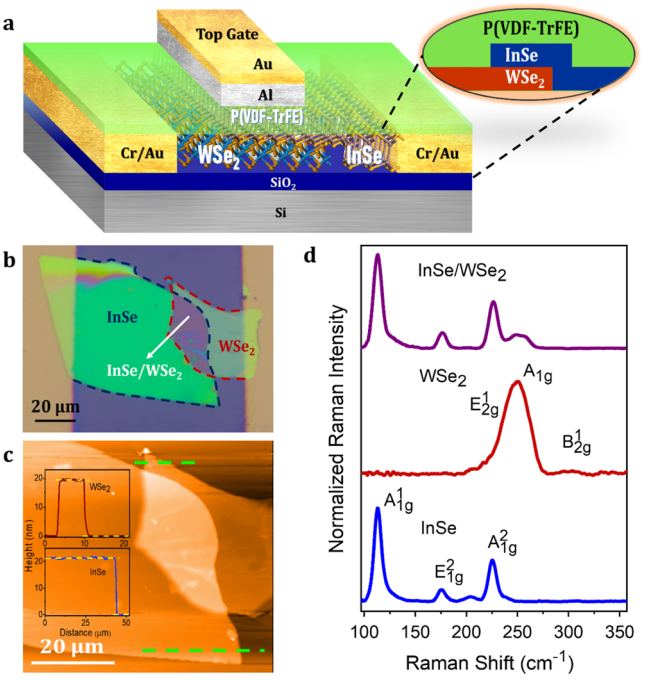

Figure 1. Device structure on a solid-state substrate. (a) Schematic representation of the P(VDF-TrFE)-coated $InSe/WSe_2$ heterostructure on a SiO_2/Si substrate. (b) Optical microscope image of the assembled heterostructure after electrode deposition. (c) AFM image of the $InSe/WSe_2$ heterostructure; the inset shows the height profile indicating the thickness of InSe and WSe_2 layers individually. (d) Raman spectra were recorded on the individual InSe, WSe_2 layers, and the assembled $InSe/WSe_2$ heterojunction.

https://doi.org/10.1021/acsami.2c22876
ACS Appl. Mater. Interfaces 2023, 15, 19121−19128

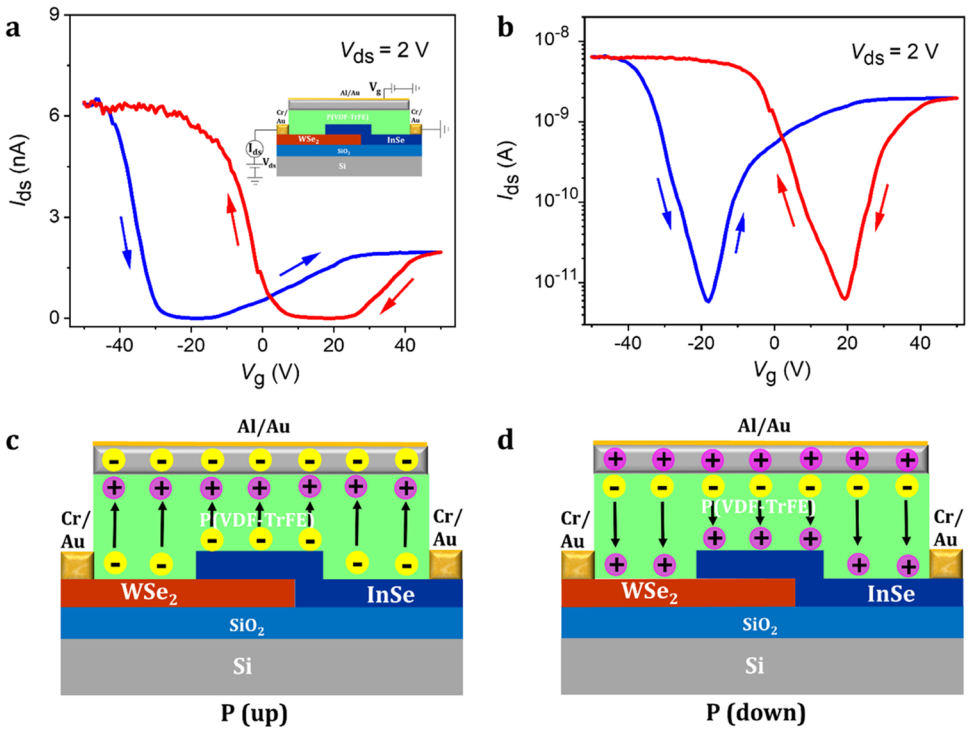

Figure 2. Transfer characteristics of the ferroelectric gated transistor. (a) Transfer curves are measured at constant V_{ds} with P(VDF-TrFE) as the top-gated dielectric and the corresponding logarithmic plot is represented in panel (b). (c, d) Schematic illustration of the ferroelectric gated InSe/WSe_2 heterostructure transistor at two different polarization states.

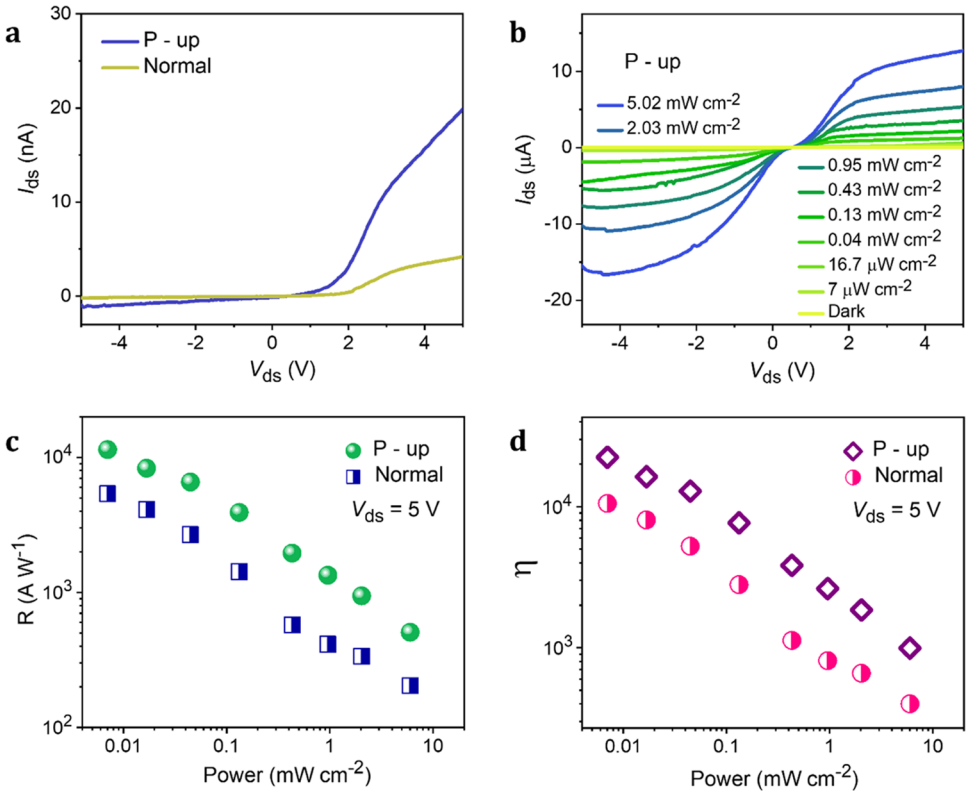

Figure 3. InSe/WSe_2 heterostructure as a ferroelectric gated phototransistor. (a) I_{ds}−V_{ds} characteristic curves of the device in the dark condition at the normal and polarized states. (b) I_{ds}−V_{ds} curves measured at the ferroelectric polarized state under 633 nm laser illumination with different power intensities. (c, d) Responsivity and photogain of the device as a function of laser power intensity at two different ferroelectric polarized states.

https://doi.org/10.1021/acsami.2c22876
ACS Appl. Mater. Interfaces 2023, 15, 19121−19128

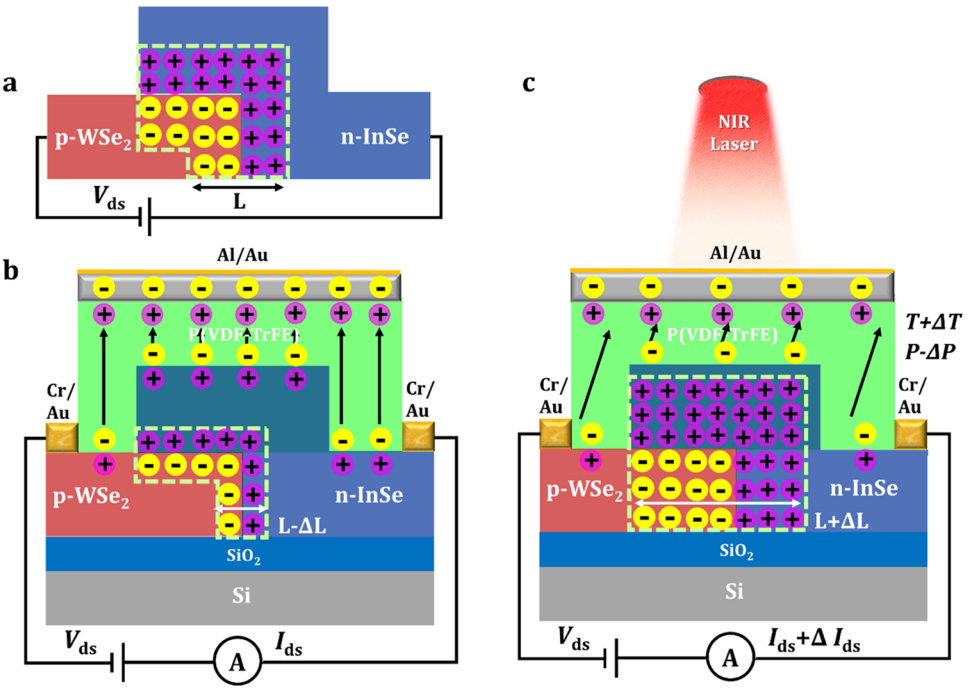

Figure 4. Schematic of the pyroelectric detector in a ferroelectric gated InSe/WSe_2 heterostructure. (a) Representation of the pn junction with p-type WSe_2 and n-type InSe without ferroelectric gating. (b) Cross-sectional illustration of the pn junction with ferroelectric P(VDF-TrFE) top-gating polarized in the upward direction. (c) Schematic depiction of a decrease in polarization in the device when irradiated with a NIR laser because of the pyroelectric effect.

transport behavior.[28,29] So, to match the n-type carrier density in InSe, we used a multilayered p-WSe_2 nanoflake. The P(VDF-TrFE) film coating with the top-gate electrode is shown in Figure S2. The Raman spectrum of the individual InSe, WSe_2 layers, and their heterojunction is represented in Figure 1d. The strong vibrational modes at 115 (A_{1g}^1 mode), 178 (E_{1g}^2 mode), and 228 cm^{-1} (A_{1g}^2 mode) in the separate InSe and the combined modes at 250 (E_{2g}^1 and A_{1g} mode) and 302 cm^{-1} (B_{2g}^1 mode) in the individual WSe_2 seem to be superimposed in the InSe/WSe_2 heterojunction, which is in accordance with the previous reports.[26,27]

Initially, before coating P(VDF-TrFE), the InSe/WSe_2 heterostructure exhibited anti-ambipolar behavior as per our previous report.[26] However, after coating P(VDF-TrFE) over the heterojunction, due to the doping effect and change in threshold voltages, the device exhibits ambipolar behavior.[30] The P(VDF-TrFE) solution was spin-coated at 3500 rpm for 20 s to obtain a thickness of 300 nm, which is well above the critical thickness (100 nm)[31] required to avoid a leakage problem. The dual sweep transfer characteristics of the InSe/WSe_2 heterostructure device are represented in Figure 2a. The nA range current can be attributed to the remote carrier scattering occurring at the semiconductor/P(VDF-TrFE) interface due to the polymer coating and the existence of the depletion region across the p-n junction. As mentioned earlier, the device exhibits ambipolar behavior, and two types of hysteresis loop are observed: one is anti-clockwise on the n-side and the other is clockwise on the p-side. Additionally, the polarization direction changes when it reaches the coercive voltage (V_c = ± 20 V), which is clear in the log plot (Figure 2b). The on/off ratio of the device estimated from Figure 2b is ~10^3, which is a considerable value in the class of 2D heterostructure-based transistors.[3,32,33] Due to the ferroelectric gating with P(VDF-TrFE), three polarization states can be observed in the device. First is the normal state without any polarization, second is the polarization up state (P-up), and third is the polarization down state (P-down), which can be obtained by poling the ferroelectric polymer with a certain voltage for 30 seconds (P-up (−50 V) and P-down (+50 V)). The schematic illustration of the polarization up and down states is depicted in Figure 2c,d, respectively.

The photodetecting performance of the device was studied by carrying out electrical measurements with laser illumination of 633 nm at different power intensities. The $I_{ds}-V_{ds}$ characteristics of the device measured in dark conditions at normal and P-up states are shown in Figure 3a. Note that if we consider a unipolar ferroelectric gated transistor, either of the up and down polarization yields higher current saturation in the ON state and the other saturates in the OFF state. So, there will be a drastic difference in the photoresponse obtained in the P-up and P-down polarization states. However, in our present study, we obtain an ambipolar transfer curve with p-WSe_2 and n-InSe heterostructure. As we can observe from Figure 2a,b, the drain source current at the P-up and P-down polarized state saturates at a higher value compared with the normal state. So, there will be a minimal difference in the photoresponse measured at P-up and P-down states. Hence, we chose to compare either of the polarized states (P-up here) with the normalized state throughout the study than with the P-down state for clarity. The electrical measurement of the device at normal and P-up states with laser illumination is represented in Figures S3a and 3b, respectively. It can be observed that the photocurrent generation is higher in the polarized state than in the normal state. The photoresponsivity (R) of the device in both states was estimated with the photocurrent (I_{ph}), incident laser power (P), and the active device area (A) using eq 1.[26,34]

https://doi.org/10.1021/acsami.2c22876
ACS Appl. Mater. Interfaces 2023, 15, 19121−19128

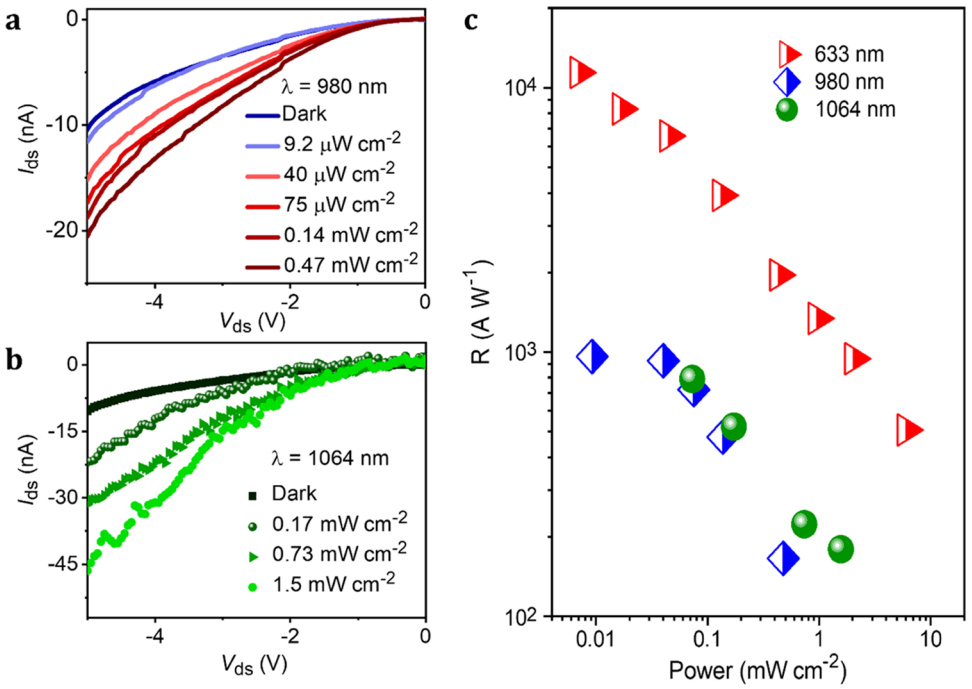

Figure 5. Ferroelectric P(VDF-TrFE) gated InSe/WSe_2 heterostructure as a pyroelectric detector. (a) and (b) I_{ds}−V_{ds} characteristic curves of the device showing a change in current when irradiated with 980 and 1064 nm laser, respectively. (c) Responsivity of the device to laser with wavelengths 633, 980, and 1064 nm as a function of the incident laser power intensity.

$$R = \frac{I_{ph}}{P \times A} \quad (1)$$

The maximum responsivity of the InSe/WSe_2 device obtained is ∼10^4 A W^{-1} in the P-up state, which is twice the responsivity obtained in the normal state, i.e. ∼5.3 × 10^3 A W^{-1} (Figures 3c and S3b). Similarly, the photogain (η) of the device determined using the equation $\eta = (Rhc)/(e\lambda)$ (h is Planck's Constant, c is the speed of light, e is the electronic charge, and λ is the wavelength of the illuminated light)[27,34] is 1.05 × 10^4 in the normal state and 2.23 × 10^4 in the P-up state (Figure 3d). The photo-switching characteristics of the device at the normal and P-up states are given in Figure S3c. In both the states, the device exhibits a stable photo-switching ability. The photoresponse time of the device under the normal state is 250 ms and under the P-up state <200 ms. The P-up state exhibits higher responsivity and photogain than the normal state because of the polarization effect. In the polarized state (Figure 2c), the holes in the InSe and WSe_2 get bound to the remnant polarization field, which reduces the depletion region and increases the conduction. Besides, the Schottky barrier formed between the material and electrode due to the difference in the Fermi level is also greatly reduced, which aids in conduction.[34] When the laser is illuminated over the device area, a large number of electron-hole pairs are generated in the material, and one of the carriers, preferably holes, here gets trapped in the remnant polarization field. This acts as a local gating while the other carrier flows through the device, which aids in the enhancement of photocurrent.[35] In addition, the device also exhibits a significant photovoltaic effect, as shown in Figure S4, where a considerable negative short-circuit current (I_{sc}) is observed with an increase in laser power intensity. The P-up state exhibits a higher short-circuit current than the normal state, indicating that the charge carrier separation is more in the P-up state, which is following the mechanism explained earlier. The above behavior provides firm evidence to support the fact that the InSe/WSe_2 area contributes more to the better photoresponse in the P-up state as the p−n junction is crucial for charge carrier separation, which aids in enhanced photocurrent.

To demonstrate IR detection in InSe/WSe_2 devices, the pyroelectric effect of the P(VDF-TrFE) is utilized. First, we exclude several possible mechanisms responsible for the IR photoresponse. The lasers 980 and 1064 nm used in this study have energies (1.26, 1.16 eV) less than the band gap of few-layered InSe (1.27 eV) and WSe_2 (1.36 eV). So, the possible origin of photoresponse to IR rays through the photoexcitation for the band-to-band transition can be ruled out. Another alternative interpretation for the photoresponse may be attributed to the photoexcitation from defect states to band transition. However, this possibility can also be excluded for the magnitude of the photoresponse is in the same order of the above band gap excitation, and the density of defect states should be much less than that of the conduction and valence bands. Hence, it clearly proves the role of the pyroelectric effect in IR detection in our study. The mechanism for IR detection using the pyroelectric effect is illustrated in Figure 4. At a reverse bias condition and thermal equilibrium without the application of any gate voltage, there is a considerable depletion region formed (assume that the length is L) with p-type WSe_2 and n-type InSe, as shown in Figure 4a. At the same reverse bias condition and thermal equilibrium but at the P-up state without NIR irradiation, the holes in the p-WSe_2 and n-InSe get bound to the polarization electric field, as depicted in Figure 4b. So, the depletion region is reduced ($L - \Delta L$) and the current flows through the device (I_{dark}). However, at a similar condition with IR irradiation, there is a localized heating effect over the polymer increasing the temperature ($T + \Delta T$). So, the polarization effect decreases ($P - \Delta P$), and the number of holes bound by the polarization electric field

https://doi.org/10.1021/acsami.2c22876
ACS Appl. Mater. Interfaces 2023, 15, 19121−19128

decreases. Consecutively, the depletion region increases (L + ΔL), and more electron-hole separation takes place, increasing the measured current (I_{ds} + ΔI_{ds}), as illustrated in Figure 4c. This overall mechanism was experimentally observed when the InSe/WSe_2 device with P(VDF-TrFE) gating was irradiated with IR lasers with wavelengths of 980 and 1064 nm. The I_{ds}−V_{ds} characteristics of the device under 980 and 1064 nm laser irradiation at different laser power intensities are shown in Figure 5a,b, respectively. There is an increase in the photocurrent observed with an increase in IR irradiation intensity, as observed from the represented graphs. The increase in temperature (ΔT) for different IR laser intensities for 980- and 1064-nm lasers is shown in Figure S5. The maximum responsivity obtained with 980 nm laser irradiation is 9.6×10^2 A W^{-1} at a laser power of 9.2 μW cm^{-2} whereas, for 1064-nm laser irradiation, it is 7.9×10^2 A W^{-1} at 0.17 mW cm^{-2}. Notably, the responsivity of the pyroelectric IR detection for the photon below the band gap of 2D materials is in the same order of magnitude as that of the normal state under the excitation of the photon energy above the band gap without the effect of pyroelectricity. To study further, the pyroelectric current was measured as a function of frequency (f) at a constant IR irradiation with 980 and 1064 nm laser, as shown in Figure S6. It can be observed that the pyroelectric current measured, $R_{py}(\omega)$, decreases with an increase in frequency, which can be fitted with the following model[36]

$$R_{py}(\omega) = \frac{X(\omega)}{\sqrt{(1 + \omega^2\tau^2)}} \quad (2)$$

where $X(\omega)$ is a polynomial term associated with the thermal effect in the pyroelectric polymer, ω is the frequency, and τ is the pyroelectric response time constant. The curves fitted with eq 2 are in accordance with the experimental data, as shown in Figure S6. The pyroelectric response time (τ) obtained for 980 and 1064 nm laser irradiation is 240 and 290 ms, respectively. According to our proposed mechanism, as the IR detection in our reported device is mainly due to the pyroelectric effect of P(VDF-TrFE), any IR laser that causes a localized heating effect upon irradiating with P(VDF-TrFE) dielectric would change its polarization, resulting in a change in the channel current in IR detection.

In addition to responsivity and photogain, specific detectivity is one of the most important figures of merit to justify the sensitivity of a photodetector. The larger the detectivity, the better it is for obtaining signals out of noises. As shown in Supplementary Note 3, the calculated detectivity for 633 nm laser illumination can reach up to about 10^{13} Jones, and IR radiation with the photon energy below the band gap of the constituent 2D materials is up to 10^{11} Jones of magnitude (Supplementary Note 5 and Figure S7), which is much better than all the previous reports of pyroelectric IR detectors, including 2D materials.[37−39] For example, the pyroelectric IR detector base on graphene/PVDF has a detectivity of only 7.42×10^6 Jones.[39] The origin of the enhanced photosensitivity can be attributed to the uniqueness of the coupling between the pyroelectricity and the built-in electric field across the p−n junction. Under IR irradiation, the increased temperature will induce the change of the PVDF polarization and, in turn, change the built-in electric field across the heterojunction. Consequently, due to the charge carriers' flow reaching a new equilibrium state, the depletion width is changed and the band alignment across the heterojunction is rearranged, which enables us to increase the charge carrier separation and enhances the photocurrent.

CONCLUSIONS

To conclude, we have demonstrated a highly sensitive photodetector based on a new mechanism of the coupling between the pyroelectric and built-in electric field for the device consisting of the 2D InSe/WSe_2 heterojunction and P(VDF-TrFE), which can detect a wide range of wavelengths covering the visible to IR spectrum. The ferroelectric polarization in the dielectric leads to an excellent photodetection in the visible range with a photoresponsivity of 10^4 A W^{-1}. On the other hand, using the heterojunction as the channel, the coupling between the pyroelectric effect of the polymer and the built-in electric field across the p−n junction extensively promoted highly sensitive IR detection. The increased temperature induces a polarization change in the irradiated area and creates charge carriers flow to establish a new equilibrium state and changes the depletion width. The specific detectivity of the IR detection is in the order of 10^{11} Jones, which is much better than all published pyroelectric IR detectors, such as the devices based on PVDF/graphene 2D materials. Thus, the coordinated benefaction from both the dielectric and the 2D heterostructure opens up multifarious possibilities for novel optoelectronic devices. For instance, with the overlap of the absorption spectrum of PVDF and black body radiation at 300 K,[34] it is foreseeable that our approach may introduce not-yet realized applications in the fields ranging from bio-imaging to military defense.

EXPERIMENTAL DETAILS

Device Fabrication. The dry transfer technique was followed to stack up the InSe/WSe_2 heterostructure. Both the crystals were mechanically exfoliated into thin flakes using a scotch tape. Initially, exfoliated WSe_2 flakes were transferred to the SiO_2/Si substrate with a PDMS stamp. In the same manner, exfoliated InSe flakes were transferred exactly to the top of the WSe_2 flake using a custom-designed micromanipulator fitted to an optical microscope (Olympus, BX 51M) with a CCD camera (Leica DFC495). After determining the thickness of the stacked InSe/WSe_2 heterostructure using the AFM technique, electrodes (Cr/Au—7/70 nm) were deposited by the thermal evaporation technique while masking the heterojunction using a Cu grid with mesh sizes ranging in the microns. For ferroelectric gating, the P(VDF-TrFE) solution was spin-coated on the device at 3500 rpm for 20 s. The pyroelectric and ferroelectric properties of P(VDF-TrFE) films were demonstrated in previous reports.[18] After baking the device in a vacuum oven at 135 °C for 2 h, Al/Au was deposited on the heterojunction area by using a custom-made shadow mask to serve as an electrode for top-gating the device.

Characterization Details. The thickness of the InSe and WSe_2 flakes was determined using a nanosurf Flex AFM (Easyscan 2V.3.1). The Raman Spectrum of the heterojunction was recorded using a micro-Raman spectrometer (Triax 550) equipped with an optical microscope (Olympus CX41) and detector (Jobin Won Horiba S Drive-500 Syncernity). The wavelength of the laser used for excitation is 532 nm. For the electrical measurements, Keithley 2636 and 2400 were employed. To measure the photoresponse of the device, an He−Ne laser with a wavelength of 633 nm was used. For IR detection, a continuous-wave 980 nm laser was used.

ASSOCIATED CONTENT

Supporting Information

The Supporting Information is available free of charge at https://pubs.acs.org/doi/10.1021/acsami.2c22876.

https://doi.org/10.1021/acsami.2c22876
ACS Appl. Mater. Interfaces 2023, 15, 19121−19128

Heterostructure assembly; microscopic images; photoresponse of the device; photovoltaic effect, and pyroelectric effect (PDF)

AUTHOR INFORMATION

Corresponding Author

Yang-Fang Chen − *Department of Physics, National Taiwan University, Taipei 10617, Taiwan; Advanced Research Centre for Green Materials Science and Technology, National Taiwan University, Taipei 10617, Taiwan;* orcid.org/0000-0003-1203-5115; Email: yfchen@phys.ntu.edu.tw

Authors

Christy Roshini Paul Inbaraj − *Department of Physics, National Taiwan University, Taipei 10617, Taiwan;* orcid.org/0000-0002-8776-9917

Roshan Jesus Mathew − *Department of Chemistry, National Taiwan University, Taipei 10617, Taiwan; Institute of Atomic and Molecular Sciences, Academia Sinica, Taipei 10617, Taiwan;* orcid.org/0000-0002-0913-6321

Raman Sankar − *Institute of Physics, Academia Sinica, Taipei 11529, Taiwan;* orcid.org/0000-0003-4702-2517

Hsia Yu Lin − *Department of Physics, National Taiwan University, Taipei 10617, Taiwan;* orcid.org/0000-0002-0886-3367

Nian-Xiu Li − *Department of Physics, National Taiwan University, Taipei 10617, Taiwan*

Yit-Tsong Chen − *Department of Chemistry, National Taiwan University, Taipei 10617, Taiwan; Institute of Atomic and Molecular Sciences, Academia Sinica, Taipei 10617, Taiwan; Department of Electrophysics, PSMC-NYCU Research Center, and LIGHTMED Laser System Research Center, National Yang Ming Chiao Tung University, Hsinchu 300093, Taiwan;* orcid.org/0000-0002-6204-8320

Complete contact information is available at: https://pubs.acs.org/10.1021/acsami.2c22876

Notes

The authors declare no competing financial interest.

ACKNOWLEDGMENTS

This work was financially supported by the "Advanced Research Center for Green Materials Science and Technology" from the Featured Area Research Center Program within the framework of the Higher Education Sprout Project by the Ministry of Education (111L9006) and the National Science and Technology Council in Taiwan (NSTC 111-2634-F-002-016, NSTC 110-2112-M-002-044). R.S. acknowledges the financial support provided by the Ministry of Science and Technology in Taiwan under project numbers MOST-111-2124-M-001-009, MOST-110-2112-M-001-065-MY3, and MOST-111-2124-M-A49-009.

REFERENCES

(1) Zha, J.; Luo, M.; Ye, M.; Ahmed, T.; Yu, X.; Lien, D. H.; He, Q.; Lei, D.; Ho, J. C.; Bullock, J.; Crozier, K. B.; Tan, C. Infrared Photodetectors Based on 2D Materials and Nanophotonics. *Adv. Funct. Mater.* **2022**, *32*, No. 2111970.

(2) Bullock, J.; Amani, M.; Cho, J.; Chen, Y. Z.; Ahn, G. H.; Adinolfi, V.; Shrestha, V. R.; Gao, Y.; Crozier, K. B.; Chueh, Y. L.; Javey, A. Polarization-Resolved Black Phosphorus/Molybdenum Disulfide Mid-Wave Infrared Photodiodes with High Detectivity at Room Temperature. *Nat. Photonics* **2018**, *12*, 601−607.

(3) Long, M.; Wang, Y.; Wang, P.; Zhou, X.; Xia, H.; Luo, C.; Huang, S.; Zhang, G.; Yan, H.; Fan, Z.; Wu, X.; Chen, X.; Lu, W.; Hu, W. Palladium Diselenide Long-Wavelength Infrared Photodetector with High Sensitivity and Stability. *ACS Nano* **2019**, *13*, 2511−2519.

(4) Long, M.; Gao, A.; Wang, P.; Xia, H.; Ott, C.; Pan, C.; Fu, Y.; Liu, E.; Chen, X.; Lu, W.; Nilges, T.; Xu, J.; Wang, X.; Hu, W.; Miao, F. Room Temperature High-Detectivity Mid-Infrared Photodetectors Based on Black Arsenic Phosphorus. *Sci. Adv.* **2017**, *3*, No. e1700589.

(5) Schwierz, F. Graphene Transistors. *Nat. Nanotechnol.* **2010**, *5*, 487−496.

(6) Xia, F.; Mueller, T.; Lin, Y. M.; Valdes-Garcia, A.; Avouris, P. Ultrafast Graphene Photodetector. *Nat. Nanotechnol.* **2009**, *4*, 839−843.

(7) Hong, X.; Kim, J.; Shi, S. F.; Zhang, Y.; Jin, C.; Sun, Y.; Tongay, S.; Wu, J.; Zhang, Y.; Wang, F. Ultrafast Charge Transfer in Atomically Thin MoS_2/WS_2 Heterostructures. *Nat. Nanotechnol.* **2014**, *9*, 682−686.

(8) Zhang, K.; Zhang, T.; Cheng, G.; Li, T.; Wang, S.; Wei, W.; Zhou, X.; Yu, W.; Sun, Y.; Wang, P.; Zhang, D.; Zeng, C.; Wang, X.; Hu, W.; Fan, H. J.; Shen, G.; Chen, X.; Duan, X.; Chang, K.; Dai, N. Interlayer Transition and Infrared Photodetection in Atomically Thin Type-II $MoTe_2/MoS_2$ van Der Waals Heterostructures. *ACS Nano* **2016**, *10*, 3852−3858.

(9) Li, A.; Chen, Q.; Wang, P.; Gan, Y.; Qi, T.; Wang, P.; Tang, F.; Wu, J. Z.; Chen, R.; Zhang, L.; Gong, Y. Ultrahigh-Sensitive Broadband Photodetectors Based on Dielectric Shielded $MoTe_2$/Graphene/SnS_2 p−g−n Junctions. *Adv. Mater.* **2019**, *31*, No. e1805656.

(10) Yuan, H.; Liu, X.; Afshinmanesh, F.; Li, W.; Xu, G.; Sun, J.; Lian, B.; Curto, A. G.; Ye, G.; Hikita, Y.; Shen, Z.; Zhang, S. C.; Chen, X.; Brongersma, M.; Hwang, H. Y.; Cui, Y. Polarization-Sensitive Broadband Photodetector Using a Black Phosphorus Vertical p-n Junction. *Nat. Nanotechnol.* **2015**, *10*, 707−713.

(11) Tong, L.; Huang, X.; Wang, P.; Ye, L.; Peng, M.; An, L.; Sun, Q.; Zhang, Y.; Yang, G.; Li, Z.; Zhong, F.; Wang, F.; Wang, Y.; Motlag, M.; Wu, W.; Cheng, G. J.; Hu, W. Stable Mid-Infrared Polarization Imaging Based on Quasi-2D Tellurium at Room Temperature. *Nat. Commun.* **2020**, *11*, No. 2308.

(12) Yu, X.; Yu, P.; Wu, D.; Singh, B.; Zeng, Q.; Lin, H.; Zhou, W.; Lin, J.; Suenaga, K.; Liu, Z.; Wang, Q. J. Atomically Thin Noble Metal Dichalcogenide: A Broadband Mid-Infrared Semiconductor. *Nat. Commun.* **2018**, *9*, No. 1545.

(13) Manga, K. K.; Wang, J.; Lin, M.; Zhang, J.; Nesladek, M.; Nalla, V.; Ji, W.; Loh, K. P. High-Performance Broadband Photodetector Using Solution-Processible PbSe-TiO_2-Graphene Hybrids. *Adv. Mater.* **2012**, *24*, 1697−1702.

(14) Yu, X.; Li, Y.; Hu, X.; Zhang, D.; Tao, Y.; Liu, Z.; He, Y.; Haque, M. A.; Liu, Z.; Wu, T.; Wang, Q. J. Narrow Bandgap Oxide Nanoparticles Coupled with Graphene for High Performance Mid-Infrared Photodetection. *Nat. Commun.* **2018**, *9*, No. 4299.

(15) Liu, Y.; Wang, F.; Wang, X.; Wang, X.; Flahaut, E.; Liu, X.; Li, Y.; Wang, X.; Xu, Y.; Shi, Y.; Zhang, R. Planar Carbon Nanotube-Graphene Hybrid Films for High-Performance Broadband Photodetectors. *Nat. Commun.* **2015**, *6*, No. 8589.

(16) Huo, N.; Gupta, S.; Konstantatos, G. MoS_2−HgTe Quantum Dot Hybrid Photodetectors beyond 2 mm. *Adv. Mater.* **2017**, *29*, No. 1606576.

(17) Xu, Z.; Zhang, Y.; Wang, Z. ZnO-Based Photodetector: From Photon Detector to Pyro-Phototronic Effect Enhanced Detector. *J. Phys. D: Appl. Phys.* **2019**, *52*, No. 223001.

(18) Chen, X.; Han, X.; Shen, Q. D. PVDF-Based Ferroelectric Polymers in Modern Flexible Electronics. *Adv. Electron. Mater.* **2017**, *3*, No. 1600460.

(19) Zhou, C.; Chai, Y. Ferroelectric-Gated Two-Dimensional-Material-Based Electron Devices. *Adv. Electron. Mater.* **2016**, *3*, No. 1600400.

(20) Sun, Z.-Y.; Li, Y.; Xu, B.; Chen, H.; Wang, P.; Zhao, S.-X.; Yang, L.; Gao, B.; Dou, X.-M.; Sun, B.-Q.; Zhen, L.; Xu, C.-Y. Tailoring the Energy Funneling across the Interface in InSe/MoS_2 Heterostructures by Electrostatic Gating and Strain Engineering. *Adv. Opt. Mater.* **2021**, *9*, No. 2100438.
(21) Xu, B.; Li, Y.; Sun, Z.-Y.; Zhao, Z.; Yang, L.; Gao, F.; Hu, P.-A.; Zhen, L.; Xu, C.-Y. Charge Transfer at the Hetero-Interface of WSe_2/InSe Induces Efficient Doping to Achieve Multi-Functional Lateral Homo-Junctions. *Adv. Electron. Mater.* **2021**, *7*, No. 2100584.
(22) Mudd, G. W.; Svatek, S. A.; Ren, T.; Patanè, A.; Makarovsky, O.; Eaves, L.; Beton, P. H.; Kovalyuk, Z. D.; Lashkarev, G. V.; Kudrynskyi, Z. R.; Dmitriev, A. I. Tuning the Bandgap of Exfoliated InSe Nanosheets by Quantum Confinement. *Adv. Mater.* **2013**, *25*, 5714−5718.
(23) Sucharitakul, S.; Goble, N. J.; Kumar, U. R.; Sankar, R.; Bogorad, Z. A.; Chou, F. C.; Chen, Y. T.; Gao, X. P. A. Intrinsic Electron Mobility Exceeding $10^3 cm^2/(V\ s)$ in Multilayer InSe FETs. *Nano Lett.* **2015**, *15*, 3815−3819.
(24) Zhou, H.; Wang, C.; Shaw, J. C.; Cheng, R.; Chen, Y.; Huang, X.; Liu, Y.; Weiss, N. O.; Lin, Z.; Huang, Y.; Duan, X. Large Area Growth and Electrical Properties of P-Type WSe_2 Atomic Layers. *Nano Lett.* **2015**, *15*, 709−713.
(25) Di Bartolomeo, A.; Urban, F.; Passacantando, M.; McEvoy, N.; Peters, L.; Iemmo, L.; Luongo, G.; Romeo, F.; Giubileo, F. A WSe_2 Vertical Field Emission Transistor. *Nanoscale* **2019**, *11*, 1538−1548.
(26) Inbaraj, C. R. P.; Mathew, R. J.; Ulaganathan, R. K.; Sankar, R.; Kataria, M.; Lin, H. Y.; Chen, Y. T.; Hofmann, M.; Lee, C. H.; Chen, Y. F. A Bi-Anti-Ambipolar Field Effect Transistor. *ACS Nano* **2021**, *15*, 8686−8693.
(27) Inbaraj, C. R. P.; Mathew, R. J.; Ulaganathan, R. K.; Sankar, R.; Kataria, M.; Lin, H. Y.; Cheng, H. Y.; Lin, K. H.; Lin, H. I.; Liao, Y. M.; Chou, F. C.; Chen, Y. T.; Lee, C. H.; Chen, Y. F. Modulating Charge Separation with Hexagonal Boron Nitride Mediation in Vertical Van Der Waals Heterostructures. *ACS Appl. Mater. Interfaces* **2020**, *12*, 26213−26221.
(28) Wu, E.; Xie, Y.; Liu, Q.; Hu, X.; Liu, J.; Zhang, D.; Zhou, C. Photoinduced Doping To Enable Tunable and High-Performance Anti-Ambipolar $MoTe_2$/MoS_2 Heterotransistors. *ACS Nano* **2019**, *13*, 5430−5438.
(29) Ren, Y.; Yang, X.; Zhou, L.; Mao, J.-Y.; Han, S.-T.; Zhou, Y. Recent Advances in Ambipolar Transistors for Functional Applications. *Adv. Funct. Mater.* **2019**, *29*, No. 1902105.
(30) Pagaduan, J. N.; Hight-Huf, N.; Datar, A.; Nagar, Y.; Barnes, M.; Naveh, D.; Ramasubramaniam, A.; Katsumata, R.; Emrick, T. Electronic Tuning of Monolayer Graphene with Polymeric "Zwitterists". *ACS Nano* **2021**, *15*, 2762−2770.
(31) Kim, K. L.; Lee, W.; Hwang, S. K.; Joo, S. H.; Cho, S. M.; Song, G.; Cho, S. H.; Jeong, B.; Hwang, I.; Ahn, J.-H.; Yu, Y.-J.; Shin, T. J.; Kwak, S. K.; Kang, S. J.; Park, C. Epitaxial Growth of Thin Ferroelectric Polymer Films on Graphene Layer for Fully Transparent and Flexible Nonvolatile Memory. *Nano Lett.* **2016**, *16*, 334−340.
(32) Ye, L.; Li, H.; Chen, Z.; Xu, J. Near-Infrared Photodetector Based on MoS_2/Black Phosphorus Heterojunction. *ACS Photonics* **2016**, *3*, 692−699.
(33) Wang, L.; Li, J. J.; Fan, Q.; Huang, Z. F.; Lu, Y. C.; Xie, C.; Wu, C. Y.; Luo, L. B. A High-Performance near-Infrared Light Photovoltaic Detector Based on a Multilayered $PtSe_2$/Ge Heterojunction. *J. Mater. Chem. C* **2019**, *7*, 5019−5027.
(34) Inbaraj, C. R. P.; Gudelli, V. K.; Mathew, R. J.; Ulaganathan, R. K.; Sankar, R.; Lin, H. Y.; Lin, H. I.; Liao, Y. M.; Cheng, H. Y.; Lin, K. H.; Chou, F. C.; Chen, Y. T.; Lee, C. H.; Guo, G. Y.; Chen, Y. F. Sn-Doping Enhanced Ultrahigh Mobility $In_{1-X}Sn_xSe$ Phototransistor. *ACS Appl. Mater. Interfaces* **2019**, *11*, 24269−24278.
(35) Konstantatos, G.; Badioli, M.; Gaudreau, L.; Osmond, J.; Bernechea, M.; De Arquer, F. P. G.; Gatti, F.; Koppens, F. H. L. Hybrid Graphene-quantum Dot Phototransistors with Ultrahigh Gain. *Nat. Nanotechnol.* **2012**, *7*, 363−368.
(36) Muralt, P. Micromachined Infrared Detectors Based on Pyroelectric Thin Films. *Rep. Prog. Phys.* **2001**, *64*, 1339−1388.
(37) Setiadi, D.; Weller, H.; Binnie, T. D. A Pyroelectric Polymer Infrared Sensor Array with a Charge Amplifier Readout. *Sens. Actuators, B* **1999**, *76*, 145−151.
(38) Chang, D. H.; Yoon, Y. S. Pyroelectric Properties of the B-Polyvilnylidene Fluoride (PVDF) Thin Film Prepared by Vacuum Deposition with Electric Field Application. *Jpn. J. Appl. Phys.* **2002**, *41*, 7234−7238.
(39) Kulkarni, E. S.; Heussler, S. P.; Stier, A. V.; Martin-Fernandez, I.; Andersen, H.; Toh, C. T.; Özyilmaz, B. Exploiting the IR Transparency of Graphene for Fast Pyroelectric Infrared Detection. *Adv. Opt. Mater.* **2015**, *3*, 34−38.

https://doi.org/10.1021/acsami.2c22876
ACS Appl. Mater. Interfaces 2023, 15, 19121−19128